International Journal of Steel Structures 17(1): 325-337 (2017)
DOI 10.1007/s13296-016-0128-2
ISSN 1598-2351 (Print)
ISSN 2093-6311 (Online)

International Journal of
STEEL
STRUCTURES
www.springer.com/journal/13296

Compression-bending Performance of L-shaped Column Composed of Concrete Filled Square Steel Tubes under Eccentric Compression

Bin Rong[1,2], Changxi Feng[1], Ruoyu Zhang[1,*], Guangchao You[1], and Rui Liu[1]

[1]*Department of Civil Engineering, Tianjin University, Tianjin, 300072, China*
[2]*Key Laboratory of Coast Civil Structure Safety, Tianjin University, Tianjin, 300072, China*

Abstract

In order to investigate mechanical properties of L-shaped column composed of concrete-filled square steel tubes (LCFT column) under eccentric compression, LCFT columns were designed and tested. Through two eccentric compression experiments, the failure mode, the curves of loading-displacement for the whole member and the curves of deflection for mono column (single limb of LCFT column) were obtained. Nonlinear finite element analysis was also employed in this investigation, in which thickness of tube flange, connecting plate thickness and diameter of the hole on connecting plate were discussed. According to results of eccentric compression test and finite element analysis, analytical method of bearing capacity of LCFT columns is proposed based on the yielding criterion of the cross-sectional edge stresses. Results of analytical method, finite element analysis and eccentric compression experiment are resistant with each other, and the accuracy of the analytical method in this paper is verified.

Keywords: L-shaped composite column, concrete-filled steel tube, eccentric compression experiment, finite element analysis, compression-bending capacity

1. Introduction

L-shaped composite column is composed of three concrete-filled square steel tubes connected by studding piece, which is usually used as corner column. It not only can save space, beautify the indoor environment, but also has better earthquake resistance and flexural properties. L-shaped composite column has gained a widespread usage in composite frame structures. As shown in Fig. 1, LCFT columns were used in post-quake reconstruction of Wenchuan, Sichuan Province, China.

As a new type of structure, there are not many studies on special-shaped column composed of concrete-filled square steel tubes. Mallikarjunal *et al.* (1992; 1994) have carried out numerical investigations on the strength of L-shaped and T-shaped short reinforced concrete columns that have been subjected to combined axial loading and bending in order to provide design aids for structural engineers. An experimental research was conducted to investigate the strength of biaxially loaded short and slender reinforced concrete columns with high strength concrete by Dundar and Tokgoz (2008; 2012), in which square and L-shaped section reinforced concrete columns were constructed and tested to obtain the load-deformation behavior and strength of columns and the test results of column specimens were analyzed with a theoretical method based on the fiber element technique. According to the experiment and theory study on L-shaped and cross-shaped column composed of concrete-filled square steel tubes of Chen *et al.* (2009) and Rong *et al.* (2012), the calculation formula of equivalent slenderness ratio was proposed, and their bearing capacity in test, superposition method and finite element analysis accord with each other well. Six specimens subjected to a constant axial load and cyclically varying lateral loading were tested by Shen *et al.* (2013) to study the effects of width to depth ratio of section, depth to thickness ratio of steel tube and axial load level on the strength, as well as stiffness, ductility and energy dissipation of concrete-filled L-shaped steel tube columns. In order to investigate the behavior of specially shaped columns composed of concrete-filled steel tube frames (SCFST frames) subjected to constant axial load and cyclically varying flexural load, Zhou *et al.* (2015) tested three specimens with two storeys

---

Received April 16, 2016; accepted September 18, 2016;

---

*Corresponding author
Tel: +86-022-27400843
E-mail: zryu@163.com

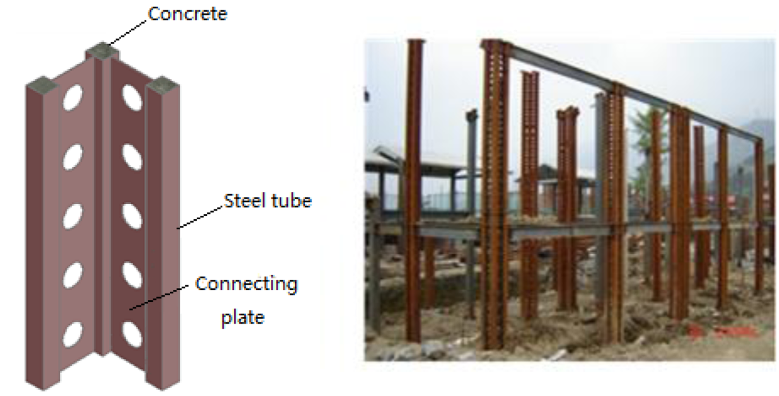

(a) L-shaped composite column (b) Project

Figure 1. L-shaped composite column.

and a single span and studied the effects of axial compression ratio and the beam-to-column stiffness ratios on the behavior of SCFST frames.

At present, the research on special-shaped column composed of concrete-filled square steel tubes mostly focus on axial compression and seismic performance, while there is a lack of information on the compression-bending performance. As a matter of fact, columns are often in compression-bending state. Therefore, it is necessary to investigate mechanical properties of special-shaped column under eccentric compression.

The objectives of this investigation include: (1) The study on the experimental behavior of L-shaped column subjected eccentric compression. (2) The investigation of the mechanical properties of L-shaped column subjected to eccentric compression by using finite element analysis. (3) The derivation of the calculation formula for equivalent slenderness ratio and the analytical method for the bearing capacity based on the experimental results and the finite element analysis.

2. Experimental Program

2.1. Test specimens

The section of L-shaped composite column is mono-symmetric. Therefore, it is necessary to take into account uniaxial bending and biaxial bending in the test (Chen *et al.* 2009). There are two specimens named GZ1 and GZ2 in the experiments, and the compression was applied on the mono column L3 in GZ1 and the columns L2 and L3 in GZ2, as shown in Figs. 2 and 3. GZ1 belongs to biaxial bending while GZ2 belongs to uniaxial bending. The sizes of two specimens are the same, and the detailed dimensions are listed in Table 1. The meaning of the symbols D, t_c, H, L, t_p, and d are shown in Fig. 3.

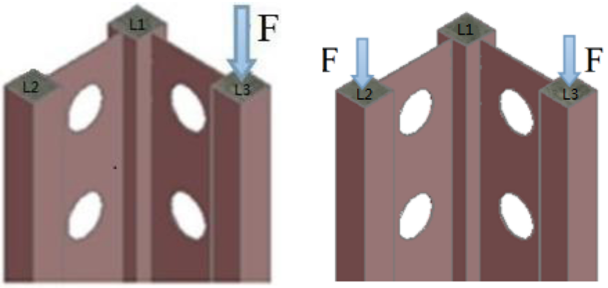

(a) GZ1 (b) GZ2

Figure 2. Force-giving method of specimens.

Table 1. Dimensions of specimens

Steel tube		Connecting plate	
$D\times t_c$ (mm)	H (mm)	$L\times t_p$ (mm)	d (mm)
80×3.75	1600	80×6	40

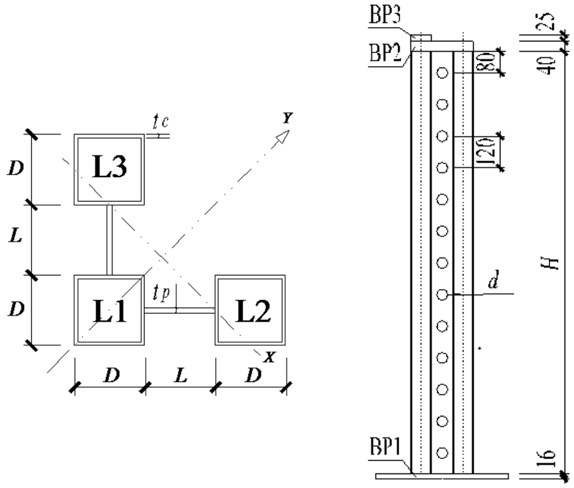

Figure 3. Configuration of specimen.

The specimens were manufactured from cold-formed square steel tubes. Connecting plates were made from steel plates. The tubes were connected with the connecting plate with fillet weld. Before concrete casting, a square steel base plate named BP1 (500 mm×500 mm×16 mm) was welded at the bottom of each specimen. The concrete was cured for 28 days. In order to apply eccentric loading on specific columns, a square steel base plate named BP2 (240 mm×240 mm×40 mm) was welded at the top of each specimen, and another one or two square steel base plates (80 mm×80 mm×25 mm) named BP3 were welded above the BP2 to bear eccentric loading, as shown in Fig. 3. In experiment, the BP1 was fixed on a dolly through two slots and the load was applied on the BP3.

2.2. Material properties

Tension coupons were cut from steel tubes and steel plates and they were tested to determine the material properties of the steel. The yield strength f_y, the ultimate strength f_u, the modulus of elasticity E_s are listed in Table 2.

Six concrete cubes with a size of 150 mm×150 mm×300 mm and six concrete cuboids with a size of 150 mm ×150 mm×150 mm were pressed under axial load after 28 days of curing in the concrete material test, from which axial compressive strength f_c and cubic compressive strength f_{cu} could be measured respectively. The measured average axial compressive strength f_c, cubic compressive strength f_{cu}, and module of elasticity E_c are listed in Table 3.

2.3. Measurement and loading

As shown in the Figs. 4 and 5, there were twelve displacement transducers (DTs) arranged at a quarter of the height, half height and three-quarters of the height of each mono column to measure the lateral displacements.

Figure 6 gives a general view of the eccentric compression test set-up. A 5000 kN capacity hydraulic testing machine was used to apply the axial compression. The compressive load and the vertical displacement were obtained from the force transducer and the displacement transducer inside the machine, respectively. Firstly a steel cleading was locked on a dolly. The specimen was then moved on the dolly and the BP1 of the specimen was fixed on the steel cleading through two slots of them. Next the dolly was moved below the hydraulic testing machine, the machine was turned on and the beam of the machine moved downwards until it was in contact with the BP3. Then scaffolds were arranged around the specimen to both install DTs and worked as the lateral support. Finally DTs were mounted on the specimen.

After the instrumentation arrangement was finished, a load increment of about 1/10 of the estimated maximum loading was applied to examine the test setup and instrumentations. The preloading ran twice cycles and then was released to zero. The loading procedure included elastic steps and inelastic steps. The elastic steps were conducted under load control at load levels from 1/10 of estimated maximum loading to 7/10 of estimated maximum loading. The inelastic steps were taken to lateral displacement levels of 2 mm each step until failure and each step was maintained for about 2 minutes. Failure means that the eccentric loading began to get down or there was such a big displacement that it was not suitable for the specimen to sustain pressure.

Table 2. Material properties of steel

Component	f_y (N/mm^2)	f_u (N/mm^2)	E_s (10^5N/mm^2)
Tube	370	512.9	2.044
Plate	373.7	467.8	2.146

Table 3. Material properties of concrete

Component	f_c (N/mm^2)	f_{cu} (N/mm^2)	E_c (10^4N/mm^2)
Concrete	27.1	38.1	3.35

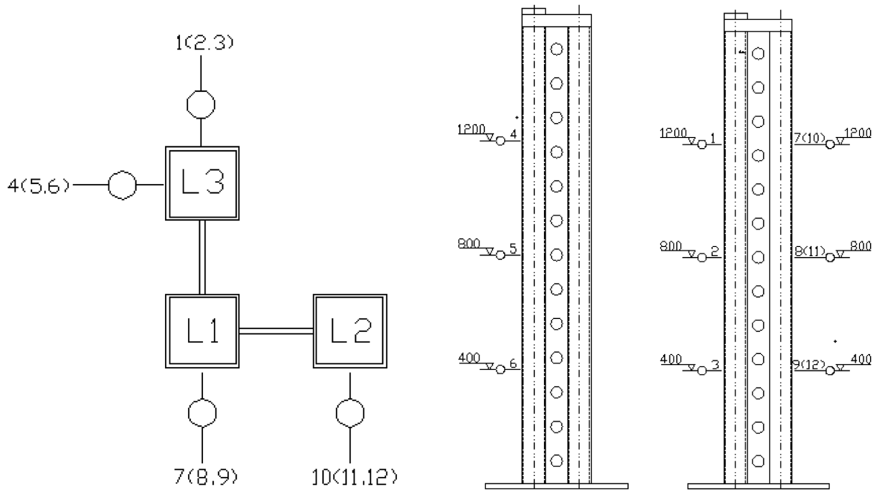

(a) Top view (b) Front view (c) Side view

Figure 4. Layout of DTs on GZ1.

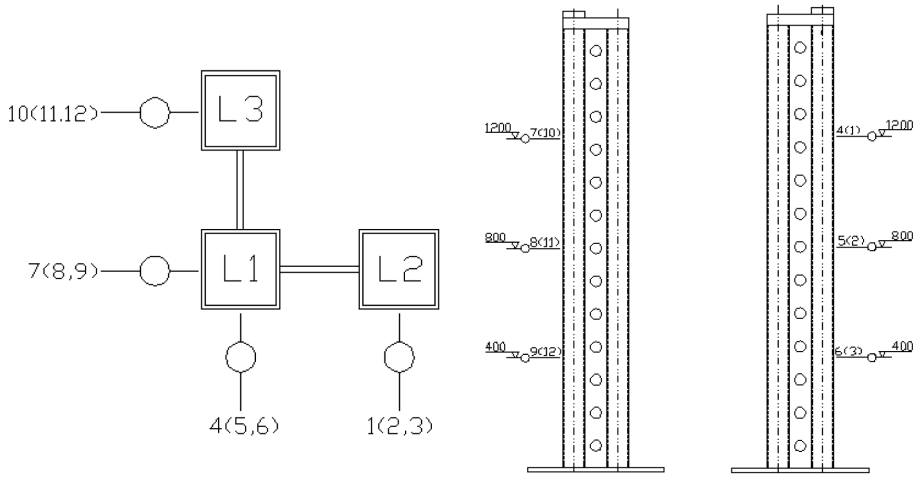

(a) Top view (b) Front view (c) Side view

Figure 5. Layout of DTs on GZ2.

Figure 6. Test set up.

(a) GZ1 (b) GZ2

Figure 7. Failure modes.

2.4. Test results and discussion

2.4.1. Failure modes

Figure 7 shows the failure modes of two tested specimens. For GZ1, during the early stage of loading, there were no obvious deformations on the specimen. When the load reached about 550 kN, GZ1 began to bend around x axis and the deflection increased apparently at the two-thirds height of the column. Then the load reached about 750 kN, an obvious trend of bending around y axis appeared on the column. As the load increased, the deformation of the column increased rapidly until failure. There was no weld failure in test, and GZ1 showed compression-bending failure as a whole. As for GZ2, there were also no obvious deformations during the early stage of loading. When the load reached about 600 kN, GZ2 began to bend around x axis and the deflection increased apparently at the two-thirds height of the column. As the load increased, the deformation of the column increased rapidly and local buckling occurred at the two-thirds height of the mono column L2 and L3 and expanded until it was failed. There was no weld failure in test, and GZ2 also showed compression-bending failure. What were different from GZ1 were that there was nearly no bending deformation around y axis during the test and local buckling appeared on GZ2. As a result, the failure mode of both GZ1 and GZ2 is global bending buckling failure as well as GZ1 belongs to biaxial bending failure, and GZ2 belongs to uniaxial failure.

2.4.2. Load-displacement curves

Figure 8 shows the load-displacement curve of two specimens. It is found that all the test specimens behave in a relatively ductile manner and testing is proceeded in a smooth and controlled fashion. All curves exhibit elastic behavior at the initial stage followed by a clear extensive plastic plateau indicating good ductility.

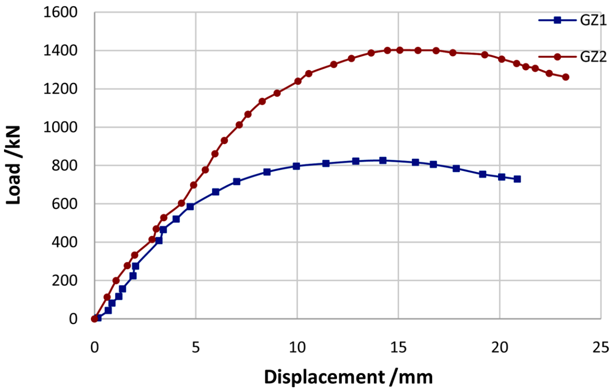

Figure 8. Load-displacement curves.

Table 4. Bearing capacity of specimens

Specimen	p_y^e (kN)	p_u^e (kN)
GZ1	550	826.4
GZ2	900	1401.7

The yield load p_y^e and the failure load p_u^e which are obtained from the load-displacement curve of each specimen are listed in Table 4. A graphical method (Nie *et al.*, 2008) is employed to catch the yield load p_y^e. The ultimate bearing loads of GZ1 and GZ2 were 826.4 and 1401.7 kN respectively. The bearing capacity of the column compressed by two side columns (L2 and L3) increased by 70% over the column compressed by one side column (L3). The stiffness of GZ2 was a little larger than that of GZ1. However, a slight increase in ductility was found in GZ1.

2.4.3. Load-deflection curves

Figures 9 and 10 show the load-deflection curves of GZ1 and GZ2 measured by DTs (Zuo *et al.*, 2012). The deflection was small during elastic stage, followed by a quick incensement in plastic stage and the deflection of

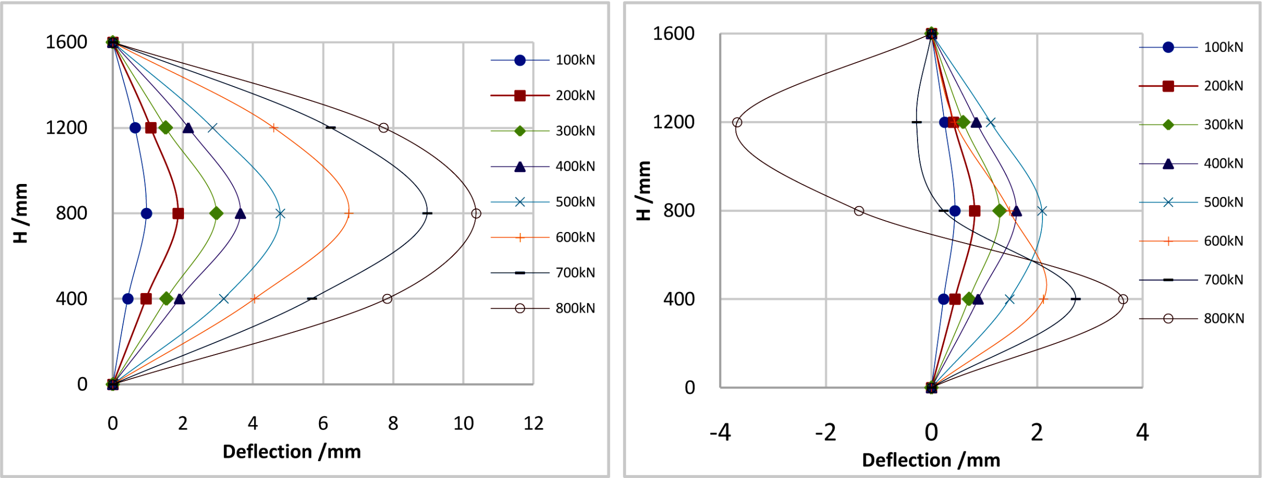

(a) DTs 1, 2 and 3 (L3)

(b) DTs 4, 5 and 6 (L3)

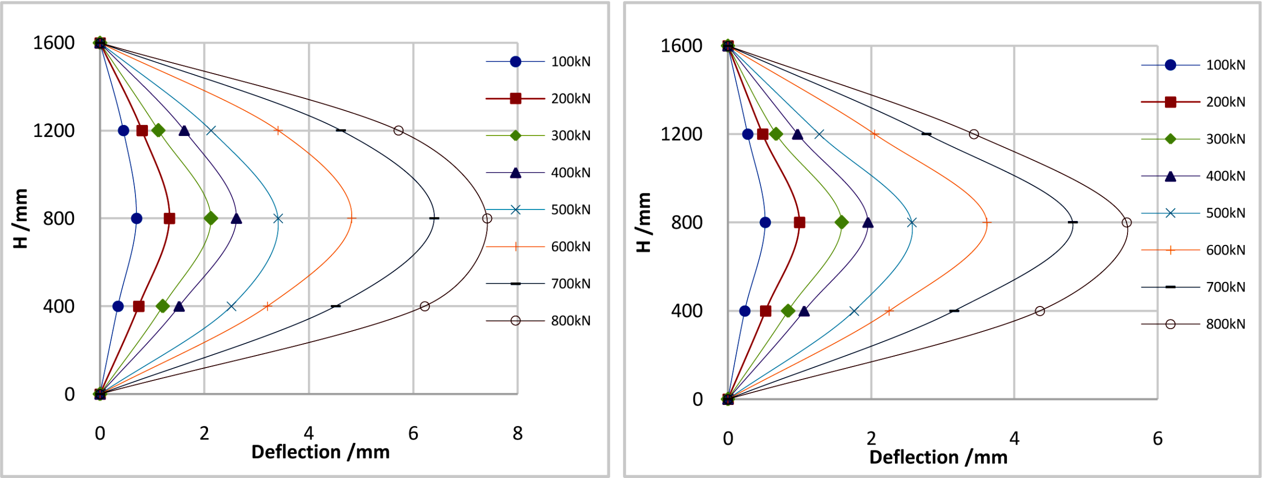

(c) DTs 7, 8 and 9 (L1)

(d) DTs 10, 11 and 12 (L2)

Figure 9. Load-deflection curves of GZ1.

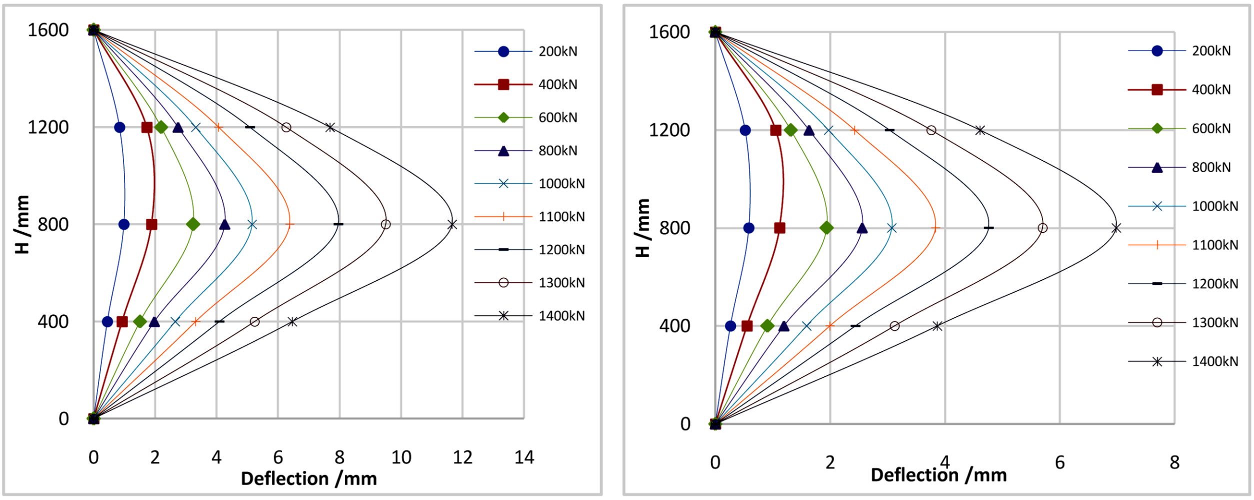

(a) DTs 1, 2 and 3 (L2) (b) DTs 4, 5 and 6 (L1)

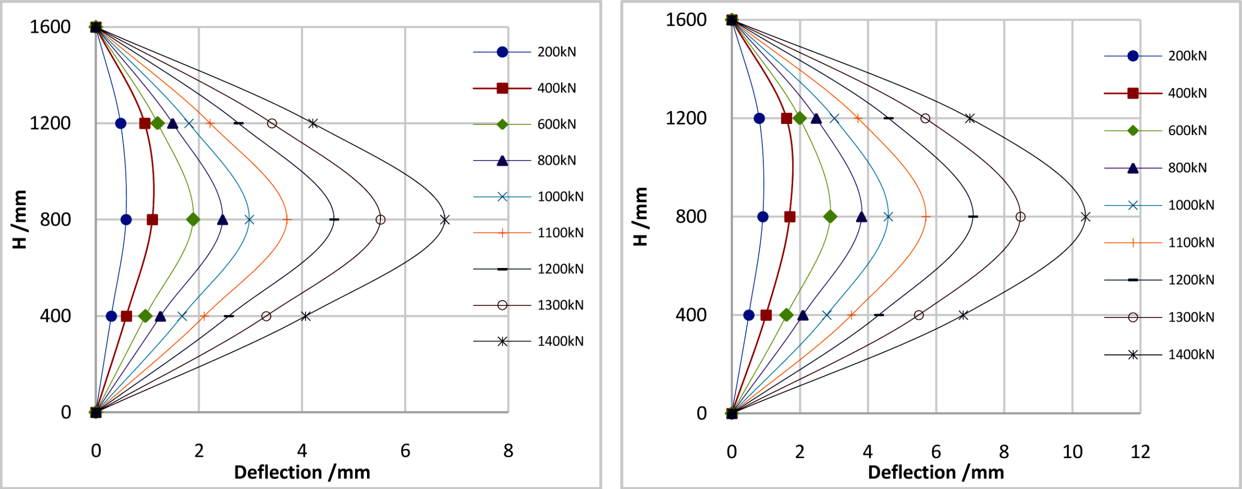

(c) DTs 7, 8 and 9 (L1) (d) DTs 10, 11 and 12 (L3)

Figure 10. Load-deflection curves of GZ2.

mono columns under compression was larger than free mono columns, which indicates that the mono column under compression took on most compression. Compared with the failure modes of specimens, it is found that the failure of specimens was induced by the mono column with large deflection. Figure 9(b) shows out-of plane bending deflection of the mono column L3 of GZ1, it appeared a slight unilateral bending deflection during elastic stage, and then it turned out to be out-of plane instability during plastic stage and expanded as load increased, which immediately resulted in the failure of GZ1.

3. Finite Element Analysis

In order to compare the experimental results with analytical predictions, parametric FEM analysis has been undertaken using the finite element package ANSYS 15.0 (Zhou *et al.,* 2015). The three-dimensional finite element models of specimens GZ1-R and GZ2-R in finite element analysis have the same size and material properties are according to the specimens in static pressure loading experiments described before. Then in this study, factors that were taken into discussion include: thickness of tube flange, connecting plate thickness and diameter of the hole on connecting plate. Key factors of different models are bold marked in Table 5.

3.1. Finite element model

3.1.1. Steel members modeling

The three-dimensional 4-node element SHELL 181 was adopted to model the steel tube and the connecting plate. Each node of the element has six degrees of freedom, three translation degrees of freedom and three translation rotation degrees of freedom. This element is capable to capture plasticity, large deflections, and large strains.

Table 5. List of analytical specimens

Specimen	Tube flange	Connecting plate	Diameter of hole	Key parameter instructions
GZ1-R	3.75	6	40	R-reference model
GZ1-HT	6	6	40	HT-heavy tube flange
GZ1-TT	2.5	6	40	TT-thin tube flange
GZ1-HP	3.75	10	40	HP-heavy connecting plate
GZ1-TP	3.75	3	40	TP-thin connecting plate
GZ1-LD	3.75	6	60	LD-large diameter
GZ1-SD	3.75	6	20	SD-small diameter
GZ2-R	3.75	6	40	R-reference model
GZ2-HT	4.5	6	40	HT-heavy tube flange
GZ2-TT	3	6	40	TT-thin tube flange
GZ2-HP	3.75	8	40	HP-heavy connecting plate
GZ2-TP	3.75	4	40	TP-thin connecting plate
GZ2-LD	3.75	6	50	LD-large diameter
GZ2-SD	3.75	6	30	SD-small diameter

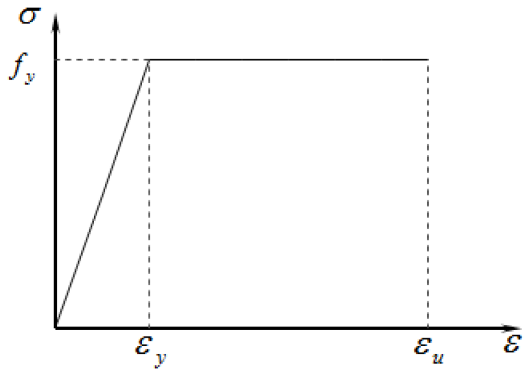

Figure 11. Constitutive law of steel members.

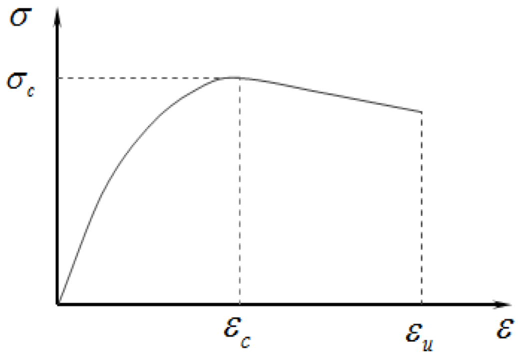

Figure 12. Constitutive law of concrete.

As shown in Fig. 11, the constitutive law of steel tubes and connecting plates was assumed elastoplastic with yielding strain ε_y equal to f_y/E_s. The strain hardening was ignored and the Poisson's ratio was equal to 0.3. The yield strength f_y was based on the coupon test. As lattice column, LCFT column can be determine to be failure when the edge of column is yielded, and because of which there is no need to consider the ultimate strength in the constitutive law. The ultimate strain ε_u was based on the elongation of steel measured by the coupon test.

3.1.2. Concrete modeling

The three-dimensional 8-node element SOLID 65 is used to model the in-filled concrete. Each node of the element has three translation degrees of freedom. This element is capable of capturing the effects of cracking in tension, crushing in compression, and plastic deformation.

The hognestad constitutive law of concrete is used for the in-filled concrete as shown in Fig. 12. The Poisson's ratio of the in-filled concrete is assumed equal to 0.2, and $\varepsilon_{c0}=1.8\sigma_{c0}/E_c$, $\varepsilon_{cu}=0.0038$. Where, σ_{c0} and E_c are axial compressive strength of concrete and module of elasticity of concrete respectively.

3.1.3. Modeling of the concrete-steel interface

The contact elements TARGE 170 and CONTA 173 are employed to model the contact action between the steel members and the concrete. These contact elements allow the surfaces to separate but not penetrate each other. They combine as a contact pair through share a real constant. The coefficient of friction between the two faces is taken as 0.25 in the analysis (Chen *et al.* 2009).

3.1.4. Modeling of loading and boundary conditions

The pressure load is transferred through square steel base plates welded at the specimen. To simulate this action the bottom of specimen is fixed and the tensile load is applied on the top side. The loads are applied as static uniform load using displacement control at each node of the loaded surfaces, and the displacement increments are identical to the increments of the static tensile loading test. The finite element models are shown in Fig. 13.

3.2. Verifications

3.2.1. Failure modes and load transfer mechanism

The predicted failure modes of specimens in two series are similar. The typical predicted failure modes and stress

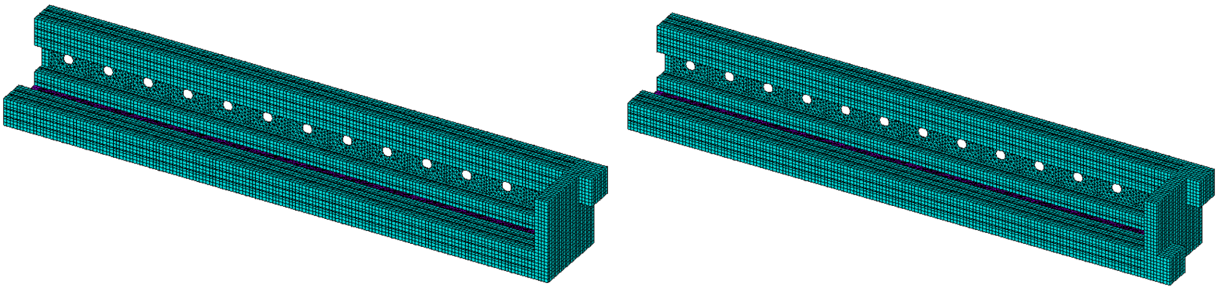

(a) GZ1 series (b) GZ2 series

Figure 13. Finite element column.

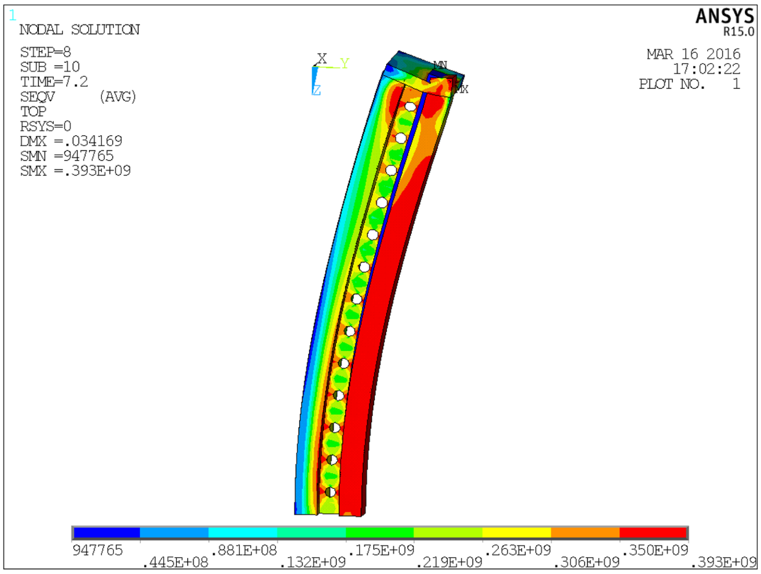

(a) GZ1-R

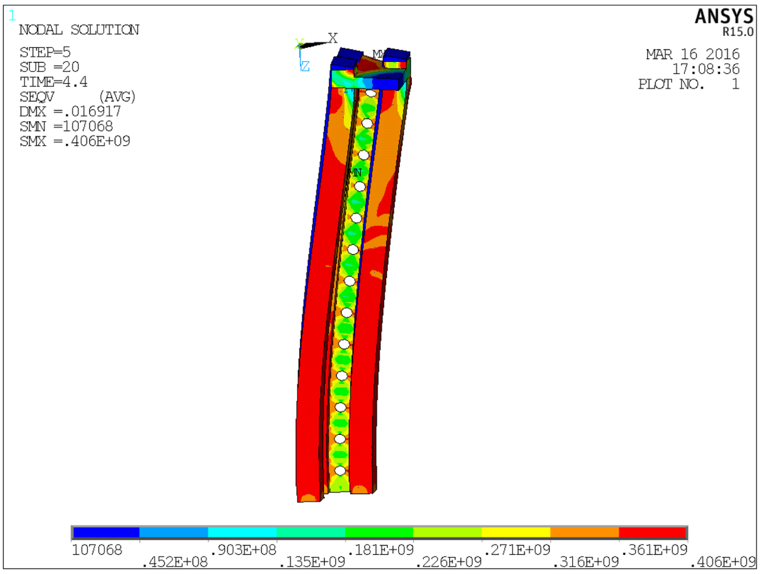

(b) GZ2-R

Figure 14. Failure modes and stress contours of specimens.

contours of specimens GZ1-R and GZ2-R are shown in Fig. 14. The numerical results indicate that both sides of column with the nearby steel tube reach the ultimate strength while stress level of the middle part of the column is lower, and it is found that the stress of the columns under compression is larger than single columns. Out-of-plane bending deformation was observed on specimen GZ1-R. The predicted failure mode demonstrates that the failure of the specimen is caused by global bending buckling. GZ1-R appears to fail by biaxial bending failure while GZ2-R exhibits uniaxial bending failure. The numerical results of specimen GZ1-R and GZ2-R are in good agreement with the static pressure test results.

3.2.2. Load-displacement curves

The load-displacement curves obtained by the finite element analysis are compared with the test curves in Fig. 15. The predicted load-displacement curves of all specimen have a linear elastic behavior at the initial stage followed by inelastic behavior when the load is further increased. All load-displacement curves are in good agreement with the experimental ones. The yield load p_y^e and the failure load p_u^e of GZ1-R and GZ2-R obtained from the predicted curves by using graphical method (Nie *et al.,* 2008) are listed in Table 6 and they are compared with the experimental ones. The analytical values are in good agreement with the experimental ones, which proves the feasibility and accuracy of the finite element analysis.

The load-displacement curves obtained by the finite element analysis are compared with each other in Fig. 16. The curves show that those initial stiffness are similar at elastic stage, due to the same beam configuration and span. Then their stiffness get changed and ultimate capacity are different from each other, indicating the influence from different connection details. GZ1-HT (GZ2-HT) has heavier tube flange while GZ1-TT (GZ2-TT) has thinner tube flange, the curve of the former is obviously higher than that of GZ1-R (GZ2-R), while the curves of the latter are lower, which indicates that the thickness of tube flange and connecting plate has significant positive influence on ultimate bearing capacity of LCFT columns. The ultimate bearing capacity of GZ1-SD (GZ2-SD) with smaller diameter of the hole on connecting plate and GZ1-HP (GZ2-HP) with heavier connecting plate is only a little larger than that of GZ1-R (GZ2-R), and that of GZ1-LD (GZ2-LD) with larger hole and GZ1-TP (GZ2-TP) with thinner connecting plate are a little larger when compared with GZ1-R (GZ2-R). Therefore, there is a negative correlation between ultimate bearing capacity of specimens and diameter of the hole, but it is not obvious.

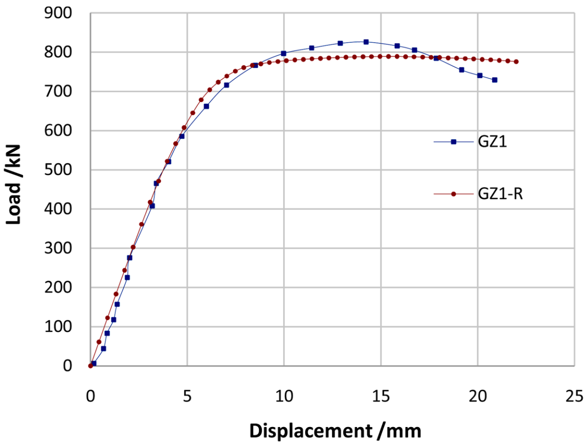

(a) GZ1 and GZ1-R

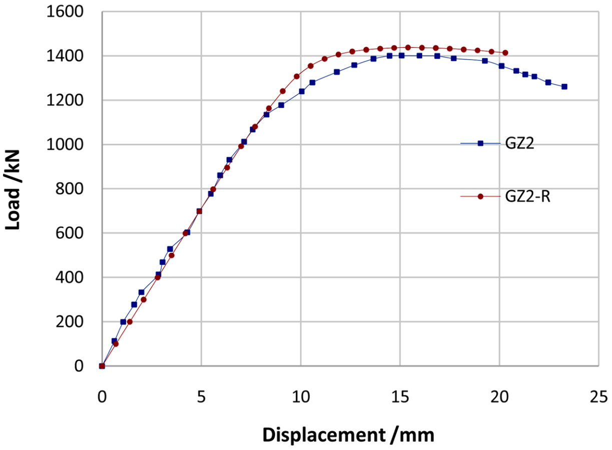

(b) GZ2 and GZ2-R

Figure 15. Comparison of load-displacement curves.

4. Theoretical Analysis

The overall agreement between the experimental and the numerical results demonstrates the feasibility and accuracy of the finite element analysis. According to results of experiments and finite element analysis, an analytical method for calculation of bearing capacity of these specimens is studied based on the yielding criterion of the cross-sectional edge stresses.

Table 6. Comparison of bearing capacity

Specimen	Yield bearing capacity			Ultimate bearing capacity		
	p_y^e (kN)	p_y^f (kN)	p_y^f/p_y^e	p_u^e (kN)	p_u^f (kN)	p_u^f/p_u^e
GZ1	550	576.3	1.05	826.4	789.1	0.95
GZ2	900	1025.8	1.14	1401.7	1438.5	1.03

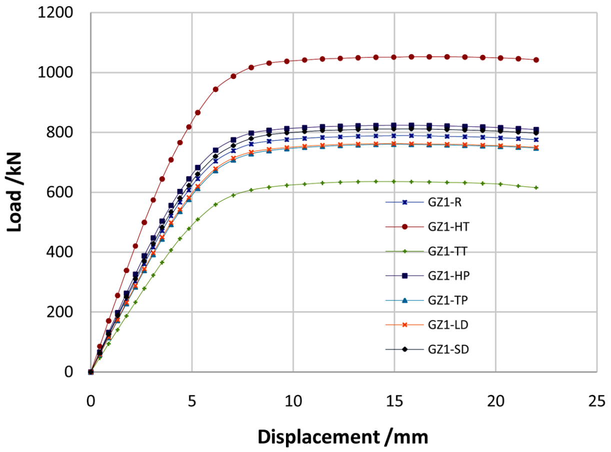

(a) GZ1 series

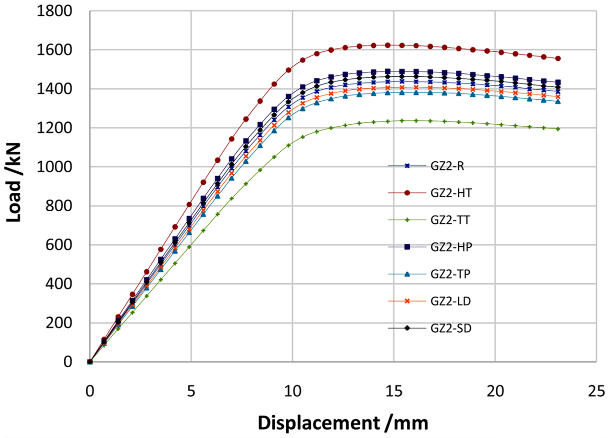

(b) GZ2 series

Figure 16. Load-displacement curves.

4.1. Compression-bending capacity

As lattice column, the stability formula of LCFT column under eccentric compression derived from the edge yield criteria (Leonard *et al.* 2005) can be classified as:

$$\frac{N}{\varphi_x A}+\frac{M_x}{W_{1x}\left(1-\varphi_x\frac{N}{N_{Ex}'}\right)}+\frac{M_y}{W_{1y}}\leq \mathrm{f} \tag{1}$$

where, $N_{Ex}'=\frac{N_{Ex}}{\gamma R}=\frac{\pi^2 EA}{1.1\lambda_{ox}^2}$, and N is the compression-bending capacity of LCFT column, φ_x is stability coefficient of x axis, A is the equivalent section area and $A=A_s+A_c\frac{f_c}{f}$, A_s is the section area of steel tubes and connecting plates, A_c is the section area of in-filled concrete, f_c is compressive strength of concrete, f is compressive strength of steel, M_x is the maximum moment against x axis, W_{1x} is the gross section modulus against x axis of the flange under larger pressure, λ_{ox} is the equivalent slenderness ratio of x axis, M_y is the maximum moment against y axis, W_{1y} is the gross section modulus against y axis of the flange under larger pressure.

LCFT column is a kind of lattice column connected by connecting plate, and both bending deflection and shear deformation of the connecting plate should be taken account in when column is subjected to compression. Therefore, it is necessary to replace the slenderness ratio with the equivalent slenderness ratio.

4.2. Equivalent slenderness ratio

4.2.1. Simplified model

Figure 17 shows the typical stress contour of the connecting plate as obtained from the finite element analysis. The stress level of the zone around the hole is higher because of stress concentration, and the rest of the area can be regarded as lateral batten plate as shown in Fig. 18, which can sustain bending moment. Consequently, a simplified model is used to derive the equivalent slenderness ratio, where the lateral batten plate model is simplified as one lateral batten plate element, and $b=1-2r$.

4.2.2. The calculation formula of equivalent slenderness ratio

Based on the theory of elastic buckling, the calculation formula of the equivalent slenderness ratio can be classified as (Leonard *et al.,* 2005, Dundar *et al.,* 2008):

$$\lambda_0=\sqrt{\lambda^2+\pi^2\gamma_1 E_s A} \tag{2}$$

where, λ_0 is the equivalent slenderness ratio, λ is the primary slenderness ratio and $\lambda=l_0/\sqrt{\frac{I}{A}}$, l_0 is the effective length of LCFT column, I is the equivalent moment of inertia and $I=I_s+E_cI_c/E_s$, I_s is the moment of inertia of steel tube section, I_c is the moment of inertia of in-filled concrete section, γ_1 is the shear deformation of column under unit force, n is the amount of square steel tube, E_s is the module of elasticity of steel, E_c is the module of elasticity of concrete. When discussing the equivalent slenderness ratio, there is not a limitation on “L”, which means that Eq. (2) can be used to calculate equivalent slenderness ratio of other kinds of special-shaped columns.

4.2.3. Equivalent slenderness ratio of flexural buckling

When the specimens bend around x axis, the cross section and the shear are symmetrical. Therefore, the semi-structure model is adopted (Chen *et al.,* 2009, Rong *et al.,* 2012).

The shear stiffness effect of the lateral batten plate model is shown in Fig. 19.

When lateral batten plate element works alone under the shear V, the shear sustained by each lateral batten plate plane V_1 is same as before so that there is bending

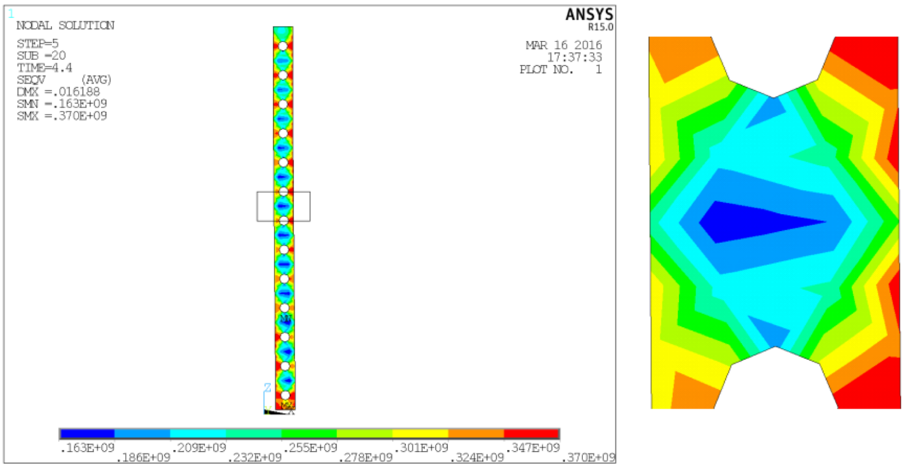

Figure 17. Von Mises stress contour of connecting plate.

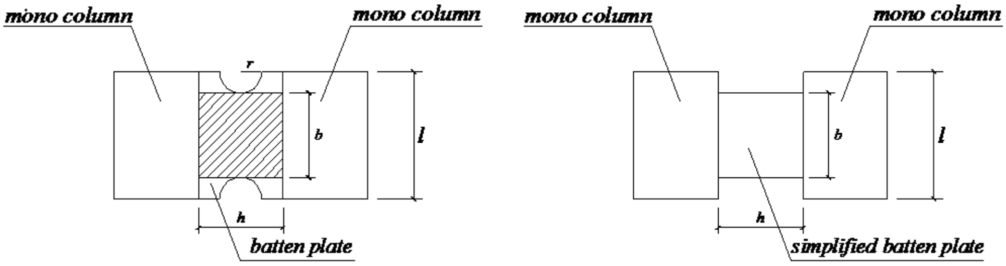

(a) Original model

(a) Simplified model

Figure 18. Simplified model of connecting plate.

moment $V_1 l/2$ on each side of lateral batten plate, therefore the rotation of each side of lateral batten plate can be calculated as:

$$\theta = \frac{V_1 lh}{12E_s I_b} \tag{3}$$

The level deformation caused by bending of batten plate δ_1 and the level deformation caused by bending of column δ_2 can be calculated as:

$$\delta_1 = \frac{\theta l}{2} = \frac{V_1 hl^2}{24E_s I_b} \tag{4}$$

$$\Delta_2 = \frac{V_1}{2}\left(\frac{l}{2}\right)^3 \frac{1}{3(E_s I_s + E_c I_c)} = \frac{V_1 l^3}{48(E_s I_s + E_c I_c)} \tag{5}$$

Then the shear deformation of column ε along y axis is obtained:

$$E = \frac{(\delta_1 + \delta_2)\cos 45^{\circ}}{l/2} = \frac{\sqrt{2}Vhl}{24E_s I_b} + \frac{\sqrt{2}Vl^2}{48(E_s I_s + E_c I_c)} \tag{6}$$

where, I_b is the moment of inertia of diagonal lacing bar section.

Therefore, the shear stiffness of the diagonal lacing bar along y axis can be classified as:

$$K = \frac{V}{s} = \left[\frac{\sqrt{2}hl}{24E_s I_b} + \frac{\sqrt{2}Vl^2}{48(E_s I_s + E_c I_c)}\right]^{-1} = \left[\frac{\sqrt{2}hl}{24E_s I_b} + \frac{\sqrt{2}l^2}{48E_s I_1}\right]^{-1} \tag{7}$$

where, I_1 is the equivalent moment of inertia of mono column and $I_1 = I_{s1} + E_c I_{c1}/E_s$.

The shear deformation of column under unit force can be calculated as:

$$\gamma_1 = \frac{V_1}{K} = \frac{\sqrt{2}hl}{24E_s I_b} + \frac{\sqrt{2}l^2}{48E_s I_1} \tag{8}$$

The equivalent slenderness ratio of flexural buckling can be calculated by using Eqs. (3) and (16).

$$\lambda_{0x} = \sqrt{\lambda^2 + \pi^2 \gamma_1 E_s A} = \sqrt{\lambda^2 + \pi^2 A\left(\frac{\sqrt{2}hl}{24I_b} + \frac{\sqrt{2}l^2}{40I_1}\right)} \tag{9}$$

where, $\pi^2/\sin^2\alpha\cos\alpha = 27$ when α ranges from 40 to 70°.

$$\lambda_{0x} = \sqrt{\lambda^2 + 0.29\lambda_1^2(1 + 2i_1/i_b)} \tag{10}$$

where, $i_1 = I_1/l$, $i_b = I_b/h$, $\lambda_1 = l/\sqrt{I_1/A}$.

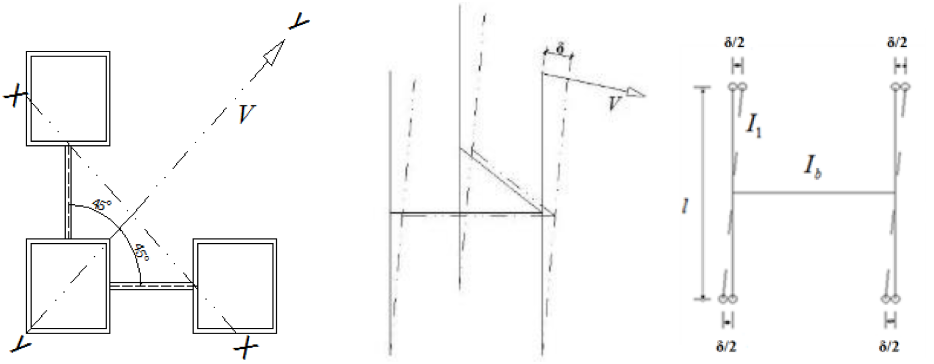

(a) Cross section (b) Shear stiffness effect (c) Semi-structure model

Figure 19. Shear stiffness effect of lateral batten plate model.

Table 7. Comparison of bearing capacity

Specimen	Ultimate bearing capacity				
	p_u^e (kN)	p_u^f (kN)	p_u (kN)	p_u/p_u^f	p_u/p_u^e
GZ1	826.4	789.1	728.6	0.92	0.88
GZ1-HT	-	1052.5	943.4	0.9	-
GZ1-TT	-	636.1	601.8	0.95	-
GZ1-HP	-	823.7	755.9	0.92	-
GZ1-TP	-	760	707.7	0.93	-
GZ1-LD	-	762.4	707.5	0.93	-
GZ1-SD	-	811.4	748.1	0.92	-
GZ2	1401.7	1438.5	1282.3	0.89	0.91
GZ2-HT	-	1623.4	1424.5	0.88	-
GZ2-TT	-	1236.8	1138.2	0.92	-
GZ2-HP	-	1460.1	1315.7	0.9	-
GZ2-TP	-	1381.8	1249.5	0.9	-
GZ2-LD	-	1408.5	1258.7	0.89	-
GZ2-SD	-	1463.3	1308.6	0.89	-

4.3. Theoretical results of compression-bending capacity

The compression-bending capacity of the specimens p_u, can be calculated by using Eqs. (1) and (10). In order to validate the accuracy of the analytical method proposed above, the ultimate bearing capacity of experiment and FEM analysis are compared with the calculated ones, as shown in Table 7, from which it can be seen that theoretical results fit well with experiment data and numerical results.

5. Conclusions

Compression-bending experiment and nonlinear FEM analysis have shown that the failure mode of LCFT columns under eccentric compression is global bending buckling failure and the columns under compression bear more load than the single columns.

Based on parametric FEM analysis, significant positive correlation has been found between ultimate the bearing capacity of specimens and the thickness of tube flange. Furthermore, it is found that the connecting plate thickness and the diameter of the hole have negative yet not too significant influence on ultimate bearing capacity of LCFT columns.

According to the results of experiments and finite element analysis, an analytical method for calculation of bearing capacity of these specimens is studied based on the yielding criterion of the cross-sectional edge stresses. The computed capacities are in good agreement with the ones obtained from experiment and FEM analysis

Acknowledgments

The research described in this paper was financially supported by the National Natural Science Foundations of China (No. 51268054 and No. 51468061) and the Natural Science Foundation of Tianjin City, China (No. 13JCQN JC07300). The financial supports are greatly appreciated.

References

Chen, Z. H., Rong B. and Fafitis A. (2009), "Axial compression stability of a crisscross section column composed of concrete-filled square steel tubes." *Mech Mater Struct.*, 4(10), pp. 1787-1799.

Dundar C., Tokgoz S., Tanrikulu AK. and Baran T. (2008), "Behaviour of reinforced and concrete-encased composite columns subjected to biaxial bending and axial load." *Build. Environ.*, 43(6), pp. 1109-1120.

Dundar C. and Tokgoz S. (2012), "Strength of biaxially loaded high strength reinforced concrete columns." *Structural Engineering and Mechanics*, 44(5), pp. 649-661.

Leonard S. and George F.(2005), Appied structural steel design, *Tsinghua University Press*, Beijing, 2005.

Mallikarjuna. and Mahadevappa P. (1992), "Computer aided analysis of reinforced concrete columns subjected to axial compression and bending, I: L-shaped sections." *Comput. Struct.*, 44(5), pp. 1121–1138.

Nie, J. G., Qin, K. and Cai, C. S. (2008), "Seismic behavior of connections composed of CFSSTCs and steel-concrete composite beams-experimental study." J. *Constr. Steel Res.*, 64(10), pp. 1178-1191.

Rong B., Chen Z. H., Fafitis A. and Yang N. (2012), "Axial Compression Behavior and Analytical Method of L-Shaped Column Composed of Concrete-Filled Square Steel Tubes." *Trans. Tianjin Univ.*, 18, pp. 180-187.

Shen Z. Y., Lei M. and Liu Y. Q. *et al* (2013), "Experimental study on seismic behavior of concrete-filled L-shaped steel tube columns." *Advances in Structural Engineering.*, 16(7), pp. 1235-1247.

Tokgoz S. and Dundar C. (2008), "Experimental tests on biaxially loaded concrete-encased composite columns." *Steel and Composite Structure*, 8(5), pp. 423-438

Zhou T., Xu M. Y. and Wang X.D. *et al* (2015), "Experimental study and parameter analysis of L-shaped composite column under axial loading." *International Journal of Steel Structures*, 15(4), pp. 797-807.

Zhou T., Jia Y. M. and Xu M. Y. *et al* (2015), "Experimental study on the seismic performance of L-shaped column composed of concrete-filled steel tubes frame structures." *Journal of Constructional Steel Research*, 114, pp. 77-88.

Zuo Z. L., Cai J., Yang C. and Chen Q. J. (2012), "Eccentric load behavior of L-shaped CFT stub columns with binding bars." *Journal of Constructional Steel Research*, 72, pp. 105-118.